ARTICLE

Nanoimprinting Techniques for Large-Area Three-Dimensional Negative Index Metamaterials with Operation in the Visible and Telecom Bands

Li Gao,[§] Kazuki Shigeta,[§] Abraham Vazquez-Guardado,[†,‡] Christopher J. Progler,[⊥] Gregory R. Bogart,[#] John A. Rogers,[§,∥,*] and Debashis Chanda[†,‡,*]

[†]NanoScience Technology Center and [‡]College of Optics and Photonics (CREOL), University of Central Florida, Orlando, Florida 32826, United States, [§]Departments of Materials Science and Engineering, Beckman Institute, and Frederick Seitz Materials Research Laboratory and [∥]Department of Mechanical Science and Engineering, University of Illinois at Urbana—Champaign, Urbana, Illinois 61801, United States, [⊥]Photronics Inc., Allen, Texas 75013, United States, and [#]Sandia National Laboratories, Albuquerque, New Mexico 87123, United States

ABSTRACT We report advances in materials, designs, and fabrication schemes for large-area negative index metamaterials (NIMs) in multilayer "fishnet" layouts that offer negative index behavior at wavelengths into the visible regime. A simple nanoimprinting scheme capable of implementation using standard, widely available tools followed by a subtractive, physical liftoff step provides an enabling route for the fabrication. Computational analysis of reflection and transmission measurements suggests that the resulting structures offer negative index of refraction that spans both the visible wavelength range (529—720 nm) and the telecommunication band (1.35—1.6 μm). The data reveal that these large (>75 cm^2) imprinted NIMs have predictable behaviors, good spatial uniformity in properties, and figures of merit as high as 4.3 in the visible range.

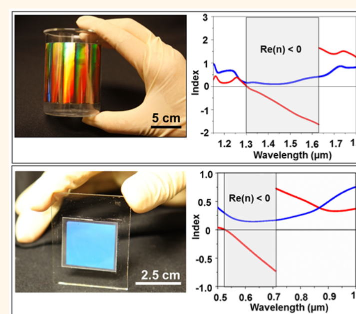

KEYWORDS: nanoimprint lithography · negative index · metamaterials

In the past decade, various important classes of negative index metamaterials (NIMs) have been experimentally demonstrated, with operation in the microwave regime,[1,2] at terahertz frequencies,[3,4] and at optical wavelengths.[5−9] Designs range from arrays of split-ring resonators to metal—dielectric—metal nanorods and, more recently, metal—dielectric—metal stacks in fishnet geometries with subwavelength dimensions. For many of the most significant practical applications, the ability to operate with high figures of merit (low loss) in the visible and telecom bands is important. Large-area, high-throughput manufacturing techniques are also required. These demands are challenging to meet, especially because the structures must incorporate nanoscale multilayer, sometimes referred to as three-dimensional (3D) unit cells, to function as an effective bulk "material". Among the various designs that have been explored, the fishnet geometry is one of the most attractive because it offers good optical properties[6,10] with options for fabrication that can be scaled from the relatively small sizes that were originally demonstrated using focused ion beam (FIB) machining[11,12] to macroscale dimensions using methods based on nanotransfer printing.[9] Here we show that the standard, widely adopted techniques of nanoimprint lithography (NIL)[13−15] can yield such types of 3D NIMs when performed with an additional subtractive, physical liftoff processing step. The results offer significantly improved properties and ability to realize structures with high figure of merit operation at wavelengths deeper into the visible than those possible with many other approaches.[5,7−9,11,12,16] NIL has been used in the past with conventional liftoff processes to fabricate single-layer, or 2D, metamaterials.[17] Three-dimensional multilayer metamaterials are different and therefore demand different approaches. This article reports successful application of nanoimprint lithography with physical liftoff as a route to such 3D metamaterials. The overall

* Address correspondence to debashis.chanda@creol.ucf.edu, jrogers@illinois.edu.

Received for review November 27, 2013 and accepted April 14, 2014.

Published online April 14, 2014
10.1021/nn5015775

© 2014 American Chemical Society

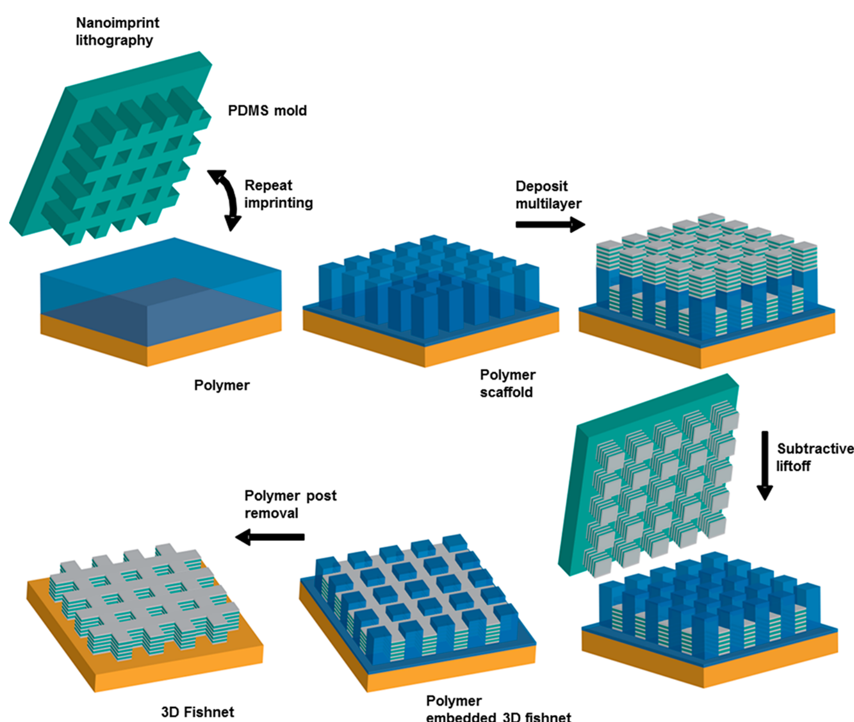

Figure 1. Fabrication of large-area 3D negative index metamaterials by combination of nanoimprint lithography and subtractive liftoff process. Schematic illustration of the steps for nanoimprint lithography and subtractive liftoff process.

sizes of the 3D NIMs and the fabrication throughputs are more than ten million (10^7) times larger than those based on focused ion beam milling[11,12] and are comparable to those enabled by nanotransfer printing.[9] Our prior publication[9] demonstrated a transfer printing technique, which is different than nanoimprinting. In particular, this past work used a multilayer metal/dielectric stack grown on a stamp, with subsequent printing of this structure to a target substrate. The process in our present article is different, but complementary, in which an imprinted polymeric pattern serves as a scaffold to grow 3D material stacks. This scheme does not involve any transfer printing step. Instead, the shape of the pattern is governed by interstitial space of the imprinted scaffold. Material grown on top of the scaffold is removed and discarded using a physical liftoff process. By comparison to nanotransfer printing,[9] the methods introduced here offer improved robustness in operation, primarily because the stack remains untouched throughout the process; only unwanted material is removed from the top of the scaffold. The process flow is quite different, in a way that enables significantly smaller dimensions and higher yields than previously possible. Improved resolution over large areas (>75 cm^2) with high figure of merit (low loss) both for telecom and visible bands represents a key consequence.

RESULTS AND DISCUSSION

Nanoimprint lithography, as used here, offers advantages over other fabrication options in terms of low-cost, high-throughput, and reliable scalability of pattern size without processing steps like exposure, development, or etching.[13,14,18] A simple modification of NIL, involving a physical liftoff process, enables large-area composite metal/dielectric structures in multilayer fishnet geometries for a class of NIMs, often referred to as 3D-NIMs. The steps for fabrication appear in Figure 1. The first involves a soft NIL process[13−15] with an elastomeric mold of poly(dimethylsiloxane) (PDMS) to form features of surface relief on a spin-cast photocurable prepolymer (NOA63, Norland) (n = 1.53; thickness ~1 μm) on a glass substrate. This implementation of NIL has been demonstrated to offer resolution that extends into the molecular size regime (*i.e.*, 1−2 nm).[19,20]

The mold in this case presents a rectangular grid pattern of narrow, raised regions with high aspect ratio, formed in a casting and curing process against a silicon master template formed by reactive ion etching with a mask of photoresist patterned by deep ultraviolet projection mode photolithography and electron beam lithography for telecom and visible band, respectively. Passing ultraviolet light through the PDMS mold while it is in contact with the liquid prepolymer cures the material into a solid form with relief in a pattern of rectangular posts in a rectangular array (*i.e.*, the inverse geometry of the relief on the PDMS). Peeling the PDMS away completes the NIL process. The lateral dimensions of the raised regions on the PDMS, which ultimately define the dimensions of the bars in the fishnet NIMs, are shown in Figure 2, where W_y and W_x are 400 and 590 nm, respectively, and the period, P, is 850 nm

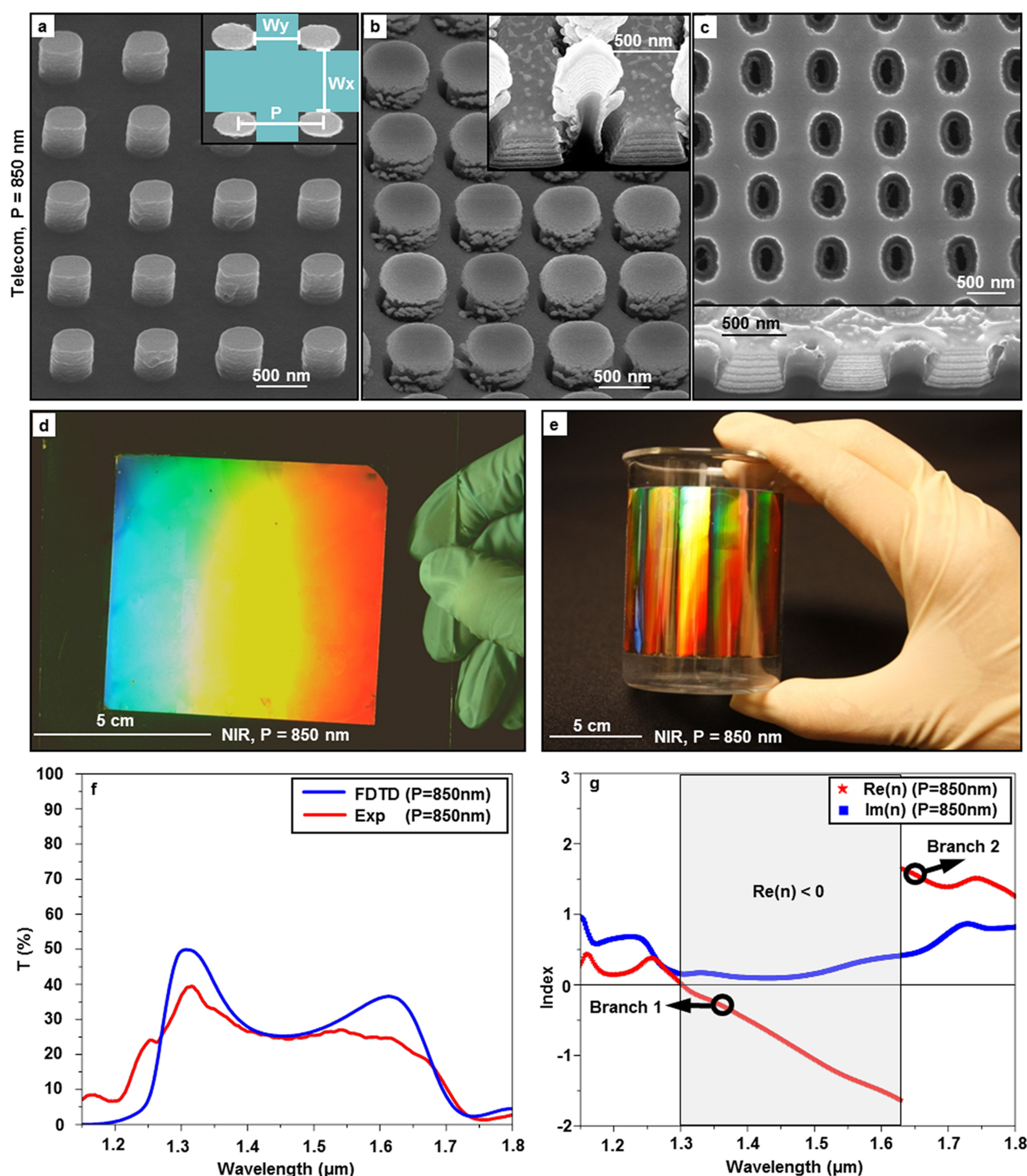

Figure 2. Large-area telecom band 3D negative index metamaterial on rigid and nonrigid substrates. Top view SEM image of nanoimprint lithography formed polymeric telecom band fishnet (*P* = 850 nm) (a) before deposition, (b) after deposition of 11 alternating layers of Ag/MgF_2, and (c) after removal of polymer posts; (c, inset) tilted view (52°) SEM image of a stack of alternating layers of Ag and MgF_2 cross sectioned by FIB. Macroscopic optical image of a large (~8.5 cm × 8.5 cm) 3D NIM on (d) rigid substrate and on (e) nonrigid substrate bent across a curvilinear surface. Experimental and FDTD results for transmission (*T*) spectra of the (f) 11-layer NIM and (g) corresponding retrieve indices showing negative index of refraction in the telecom band.

for NIMs that operate in the telecom band (Telecom); W_y and W_x are both 120 nm, and P is 300 and 400 nm for NIMs that operate in the visible (VIS) band, obtained from finite difference time domain (FDTD) simulations. Previous experimental and theoretical results on related multilayer fishnet metamaterials[6,9,10,12] provide context for the present work, which focuses on an advanced technique for large-area nanofabrication. Next, a thin protective layer of fluorocarbon CF_n is introduced with a C_4F_8 fluorination step[21] to reduce the adhesion between the polymer template and deposited materials. Collimated deposition of 11 alternating layers of silver (Telecom = 45 nm, VIS = 35 nm) and magnesium fluoride (MgF_2) (Telecom = 45 nm, VIS = 15 nm) by electron beam evaporation onto the nanoimprinted polymer forms physically separated multilayer stacks on the raised and recessed regions. Silver offers relatively low loss compared to other metals in the optical domain, and it can be deposited easily using electron beam evaporation. MgF_2 is a widely used class of transparent optical material and is frequently found in various optical coatings.

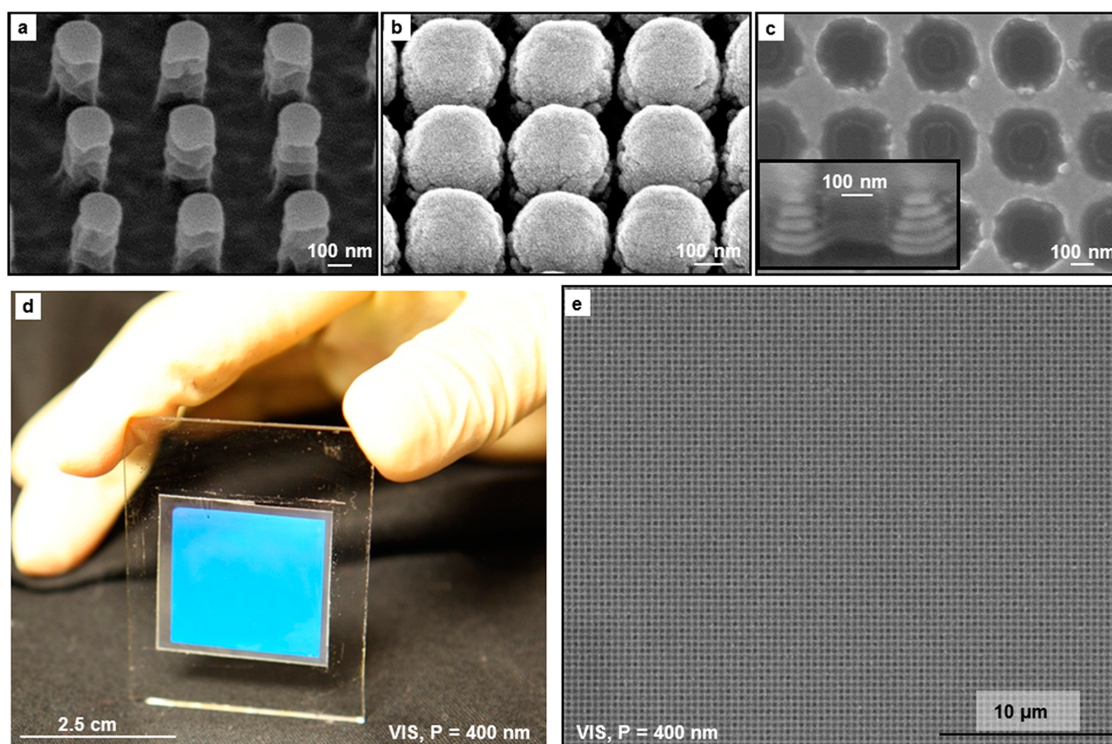

Figure 3. Large-area visible 3D negative index metamaterial. Top view SEM image of nanoimprint lithography formed polymeric visible fishnet (P = 400 nm) (a) before deposition, (b) after deposition of 11 alternating layers of Ag/MgF_2 layers, and (c) after removal of polymer posts; (c, inset) tilted view (52°) SEM image of a stack of alternating layers of Ag and MgF_2 cross sectioned by FIB. Macroscopic optical image of a large (~2.5 cm × 2.5 cm) 3D NIM (d) and corresponding large-area top view SEM is shown in (e).

The choice of an 11-layer stacked architecture provides a thickness regime that offers "bulk"-like optical response (>7 layers)[6,9,10,12] but at the same time is sufficiently thin to allow easy fabrication using our approaches, without significant consequences of nonvertical film growth. A bilayer of Ti (5 nm) and SiO_2 (30 nm) evaporated on top of these stacks prepares the substrate for the next step of the fabrication, which is critically important in the scheme described here. Contact of a uniform slab of PDMS activated to generate hydroxyl functionality on its surface leads to condensation reactions that bond the PDMS to the SiO_2 to yield strong adhesion. Physically peeling the PDMS away removes selectively the multilayer stacks on the raised regions. The result of this subtractive, physical liftoff process is a fishnet NIM structure, corresponding to multilayers deposited only into the recessed areas (detailed process steps appear in Supporting Information Figure S1). As a final procedure, oxygen plasma etching removes the polymer posts that exist in the holes of this mesh. The key distinction of this approach, compared to the nanotransfer printing process described previously, is that the materials that form the 3D-NIMs are not manipulated by transfer. This difference leads to improved yields and resolution.

Representative results appear as SEM images in Figure 2a–c and Figure 3a–c for both Telecom and VIS geometries, respectively. The left set of images corresponds to the nanoimprinted polymer (Figure 2a Telecom and Figure 3a VIS); the middle images show the sample after deposition of 11 layers of Ag/MgF_2 and a top bilayer of Ti/SiO_2 (Figure 2b Telecom and Figure 3b VIS); and the right set of images (Figure 2c and Figure S3 Telecom and Figure 3c VIS) shows fishnet NIMs in the recessed regions of the nanoimprinted polymer, after physical liftoff of the top layers and removal of exposed polymer posts with reactive ion etching. The multilayer deposit shows expected angular growth (12–15°)[9,22,23] such that stacks on the polymer posts exhibit mushroom-like shapes in which new layers sequentially overhang previous layers. Shadowing from the top layers leads to fishnet NIMs in the recessed regions, with sharply defined edges and overall trapezoidal cross sectional shapes. In the Telecom case, the bottom fishnet begins with W_y/W_x = 400 nm/590 nm at the base and ends with W_y/W_x = 190 nm/380 nm at the top (Figure 2c). For the VIS case, the base and top have $W_y = W_x$ = 120 nm and $W_y = W_x \sim$ 15 nm, respectively (Figure 3c). These selections of line widths are based on engineered optical responses as described in the following section. As shown in the SEM images of Figure 2c and Figure 3c, the subtractive liftoff process yields well-defined fishnet NIMs with high levels of structural uniformity. Observed ~5–10% variations in fishnet line widths (W_x and W_y) arise primarily from variations in angular stack growth. Negligible line width variation arises from the NIL process. Figure 2d,e shows optical images of

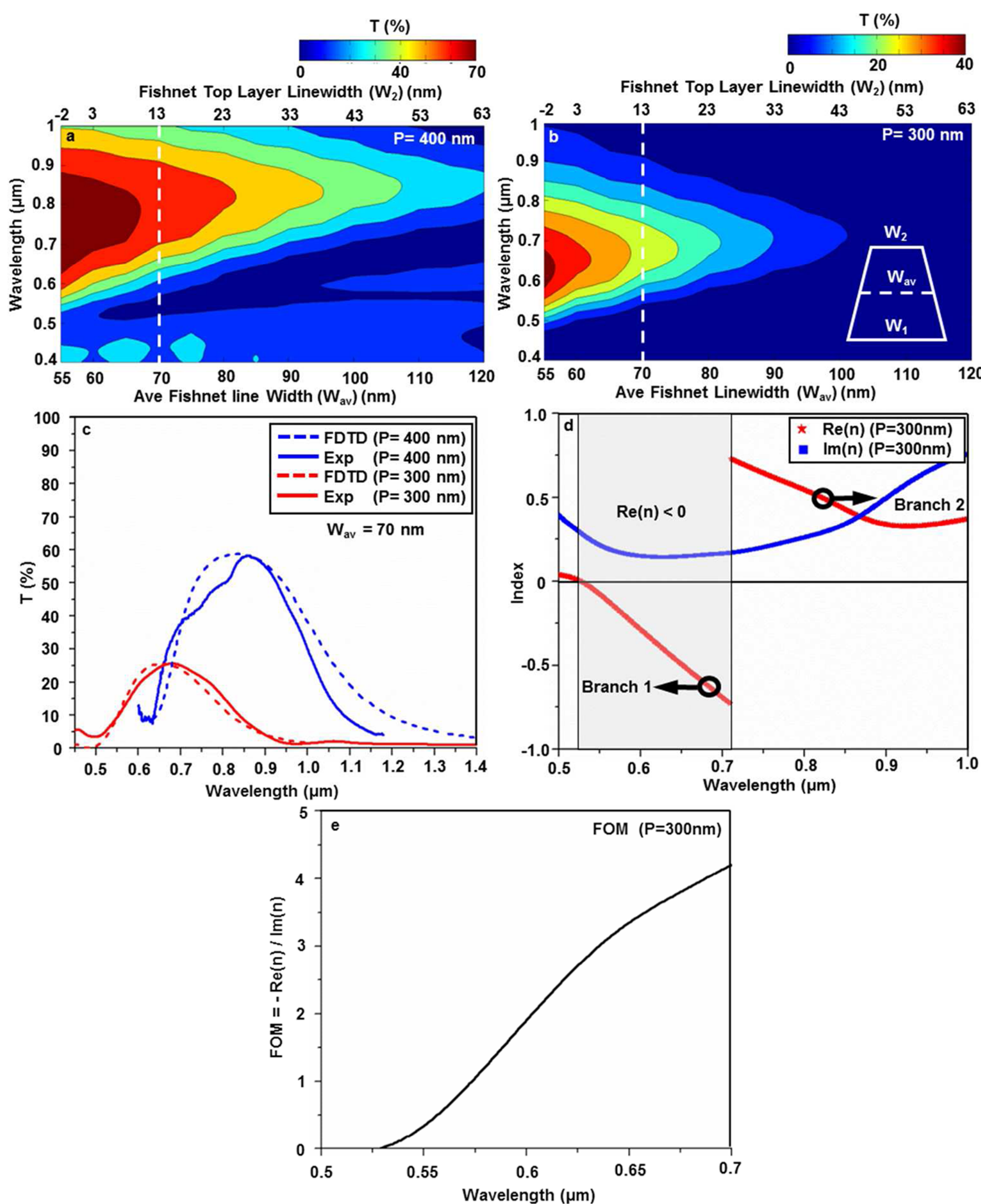

Figure 4. Experimental measurements and simulation results for transmission and refractive indices of 3D visible negative index metamaterials. FDTD-predicted transmission as a function of depth-averaged fishnet line width (W_{av}) for (a) $P = 400$ nm and (b) $P = 300$ nm. (c) FDTD-predicted and experimentally measured transmission for the chosen depth-averaged fishnet line width $W_{av} = 70$ nm and the corresponding (d) retrieved refractive indices and (e) FOM for $P = 300$ nm fishnet.

large-area (~75 cm^2) Telecom NIMs on a flat substrate and after bending to conform to a curved surface. A corresponding VIS ($P = 400$ nm) sample (also large area (~6.5 cm^2) and with 11 layers) appears in Figure 3d. In both examples, the sample areas are limited only by the sizes of the PDMS molds and not by any intrinsic constraint associated with the process. An important aspect of this fabrication scheme is that the critical patterning step can be conducted with widely available, commercial tools for NIL, unlike the more specialized systems required for nanotransfer printing.

Optical characterization reveals a broadband transmission peak at 1.35 μm for the $P = 850$ nm telecom band 11-layer 3D fishnet as shown in Figure 2f. The results exhibit good agreement with finite difference time domain prediction. Figure 2g shows the real and imaginary components of refractive index extracted by FDTD.[24−26] For the present case, experimentally measured transmission and reflection data are matched with FDTD predictions of the structure with the same dimensions. FDTD-predicted transmission/reflection amplitude and phase are used for extraction of refractive indices. It has been firmly established in the optics community that 3D full-vectorial finite difference time domain prediction of index is sufficiently accurate for experimental observations.[24−26] Interferometric measurements verify such FDTD predictions of negative refractive index in related, small-area samples.[11,12] The real part of the refractive index (Re(n)) determined by FDTD is negative between 1.35 and 1.6 μm with a

maximum of −1.7 at a wavelength of 1.6 μm. At 1.6 μm, the real component of index changes sign from negative to positive where "Branch 1" and "Branch 2" as labeled in Figure 2g represent two different propagating modes. The refractive index is a continuous function of wavelength for a given propagating mode inside a structure. For the present NIM, two segments of refractive index, labeled as Branch 1 and Branch 2, represent two different propagating modes inside the multilayer stack.[6,9,10,12] This behavior has been reported in other related structures.[6,9,10] The mode (Branch 1) that possesses negative index (Re(n)) achieves −1.7 at 1.6 μm. The optical responses of such metamaterial structures are governed by anomalous dispersion when the refractive index is between 0 and 1.[27] For the present case at around 1.1 μm wavelength, the transmission and reflection are both low. Here, energy is dissipated as metallic loss. The exact loss mechanism for materials with near zero (DC zero frequency) and less than one (superluminal group velocity) refractive index is the subject of intense research within the broader community.

For the VIS structure, the design goal was to shift the negative index band deep into the visible wavelength range while maintaining high levels of transmission. Studies using FDTD indicate that both requirements scale together; that is, narrower fishnet line width (W_x) enhances transmission, and also the transmission peak moves to lower wavelength range due to excitation of symmetric plasmonic resonances at metal/dielectric interfaces, as can be observed in Figure 4a,b for P = 400 and 300 nm fishnets, respectively. Experimentally, this type of operation can be achieved by reducing the line width ($W_x = W_y = W_1$) of the fishnet scaffold by changing dimension of the NIL mold. Effects of angular growth limit the average stack line width W_{av} to 70 nm, corresponding to line widths of $W_2 \sim 15$ nm and $W_1 \sim 120$ nm at the top and the base of the structure, respectively (Figure 4b). Optical characterization reveals broadband transmission peaks at 850 and 650 nm for 11-layer 3D fishnets with P = 400 and 300 nm, respectively, as shown in Figure 4c. Previous results indicate that at least three unit cells are needed to achieve a bulk-like negative index response.[6,9,10] Hence, for the present case, 11 alternating metal/dielectric layers are sufficient to experimentally and computationally achieve a 3D metamaterial response. Parameter extraction by FDTD indicates that the P = 300 nm structure has a negative index between 529 and 710 nm with a maximum of −0.73 at a wavelength of 710 nm (Figure 4d). The maximum negative index achieved in the present case is −0.73, which indicates a group velocity that can exceed the speed of light in free space[12] due to the nature of wavelength-dependent dispersion of the propagating mode. The vertical stacking of layers in this class of metamaterial yields negative index of refraction only along the normal angle of incidence, and hence all optical measurements were performed at normal incidence for the present case.[6,9−12] The full tensorial nature of the optical properties is discussed in recent work.[28] An important optical property of a negative index metamaterial is its loss. The losses for these types of structures are typically reported in terms of a figure of merit (FOM) defined by −Re(n)/Im(n). The maximum FOM for the visible (P = 300 nm) NIM is 4.3, as shown in Figure 4e. The wavelengths and the figures of merit are shorter and higher, respectively, than those previously achieved in related, multilayer 3D-type NIMs.[12]

The measured and FDTD-predicted transmission (T) for the telecom band metamaterial differ slightly, likely due to angular growth and associated complex contours at the edges of the metal/dielectric stacks. The agreement is significantly better for the VIS sample (Figure 4c) due to reduced impact of angular growth in the small feature sizes associated with this structure. We do not observe significant changes in transmission due to the presence of the substrate or the slight tapered geometry of the stack, consistent with previous results.[12] Hence, we used a bianisotropy coefficient of unity during parameter extraction. A key feature of the fabrication approaches described here is that they avoid etching steps that can otherwise lead to detrimental parasitic effects associated with sidewall roughness and/or introduction of foreign chemical species.

CONCLUSIONS

The results described here demonstrate that simple NIL techniques, when combined with a physical liftoff process, provide access to large-area, high-quality 3D metamaterials. The reported NIMs operate in wavelength regimes shorter than those previously possible using nanotransfer printing, an alternative large-area patterning approach. The practical ease and wide availability of the NIL procedures and the liftoff processes, their ability to accommodate both critical feature sizes deep into the nanometer range and macroscale areas, and their compatibility with wide ranging classes of materials represent a combination of attributes that suggest a strong potential for use in both engineering development and exploratory research in fishnet and other emerging classes of metamaterials.

METHODS

Fabrication of Silicon Master Templates and PDMS Molds. The silicon daughter master pattern was etched using a Bosch process (94 mTorr, etch/passivation: cycle time, 5 s/5 s; RIE power, 20 W/0 W; SF_6/C_4F_8 flow rate, 35 sccm/110 sccm for constant ICP power of 600 W; etch rate 1 μm/80 s) with SF_6 gas, to a depth between

600 and 700 nm, through a combination of Si_3N_4 layer and photoresist mask formed by soft nanoimprint lithography.[9] Controlling the etching conditions allowed variation of fishnet line widths (W_x and W_y). The original large-area master pattern was defined on a silicon wafer by deep ultraviolet projection mode photolithography and electron beam lithography for telecom and visible band, respectively. Use of electron beam lithography and glass etching methods employed by Photronics Inc. allows for larger structures with fine feature size to be more easily fabricated. Leveraging current infrastructure for the semiconductor industry reduces development costs for proof of concept. The molds for this process consisted of elements of PDMS (Dow Corning, Sylgard) formed by casting and curing against the large-area silicon master. Many molds can be produced from one silicon master.

Nanoimprint Lithography. We used a commercially available photocurable polyurethane material (NOA 63, Norland Inc.) for the NIL resist. A liquid prepolymer of this material was drop-cast onto a clean glass substrate. Next, a high aspect ratio PDMS mold was pressed against the liquid, and any trapped bubbles were allowed to permeate through the PDMS. Passing UV light (Osram Sylvania 100 W MV PAR38, power density 8.4 mW/cm^2) through the PDMS while in contact with the NOA for 1 h cures the NOA into a solid form. The PDMS mold was then peeled away to complete the NIL process. Next, the imprinted NOA was fluorinated by exposure to C_4F_8 in an ICP-RIE system (SPTS Inc., RIE power = 0 W, ICP power = 600 W, 15 s, chamber pressure = 94 mTorr, C_4F_8 flow rate = 110 sccm) which formed a cross-linked polymer on the surface to reduce the surface adhesion.

Collimated Deposition of Multilayer Stacks by Electron Beam Evaporation. Multilayer stacks were deposited using a Temescal (FC-1800) six-pocket electron beam evaporation system. For optimal collimation, a small filament (6 mm) was used; the sample was mounted perpendicular to the flux from the source, and the distance between the sample and source was maximized (~2 ft). For deposition of Ag, MgF_2, Ti, and SiO_2, average chamber base pressures of 1.5×10^{-6} Torr and deposition rates of 0.1−0.15 nm/s were found to yield the best results.

Subtractive Liftoff. A low modulus, tacky form of PDMS, created by mixing in a 25:1 ratio by weight base and curing agent of a commercial material (Sylgard 184, Dow Corning), was used for the liftoff slab. The surface of this material was activated by exposing it to ozone created by deep ultraviolet light (BHK Inc., grid lamp, model 88-9102-02) for 3.5 min. Contact with the surface of multilayer stack condensation reactions between the hydroxyl groups on the PDMS and those on the top exposed layer of SiO_2 on the substrate led to strong adhesion. Peeling the PDMS away physically removes the stacks, in their entirety, from raised regions of the substrate. The NOA scaffold was removed by oxygen reactive ion etching (PlasmaLab Master Slave dual-chamber reactive ion etcher, power = 50 W, pressure = 50 mTorr, flow rate = 50 sccm, time = 300 s). The results leave a fishnet multilayer stack at the recessed regions.

Optical Measurements. Transmission/reflection spectra were collected using a 4×−4×, 0.1 numerical aperture objective on an optical microscope (Hyperion 1000) coupled to a Fourier transform infrared spectrometer (Vertex 70) and outfitted with a spatial aperture with a diameter of 3.75 mm. Reflection spectra were normalized to a silver mirror with 96% reflectivity. Transmission spectra were normalized using a bare substrate.

FDTD Simulation. Transmission and reflection spectra were calculated using experimental parameters for the printed 3D NIM structures, with commercial FDTD software package (Lumerical, Lumerical Solutions Inc.). A Drude model was used for the dielectric parameters of silver in the FDTD simulation, with a plasma frequency of 1.37×10^{16} s^{-1} and scattering frequency of 85×10^{12} s^{-1}. The scattering frequency was increased by a factor of 3 compared with that of bulk silver to account for the additional surface scattering loss. The FDTD simulations used averages of transmission/reflection separately computed with plane wave sources of TE and TM polarizations to compare with the unpolarized light used in the spectrometer. In particular, due to our present optics, our microscope-coupled FTIR system (Bruker Vertex 70-Huperion 1000) is capable of making high-quality transmission and reflection measurements without polarizer−analyzer arrangement. To remain consistent with measurements, we used averaging of TE and TM polarization to achieve the response of an unpolarized light in FDTD simulation. These simulations used precise geometries extracted from images such as the one in Figure 2c and Figure 3c, but without any line edge roughness (LER). The partial infiltration of openings in the mesh structure with adhesive material (NOA) used in the NIL process increases the background refractive index, n_s. The effect moves the optical response to higher wavelength range compared to the case with air as the background medium.[6] In the proposed technique, the 3D multilayer stack is embedded and supported inside a polymeric scaffold. An O_2 plasma etch removes the polymeric scaffold in the exposed regions. The effective index of the surroundings is defined by the polymer that remains. This value corresponds to n_s. The best match between FDTD and experiment occurs between n_s = 1.2−1.3. We used $n_s \sim 1.25$ and 1.2 for telecom and visible bands respectively in the FDTD modeling (greater polymer infiltration inside larger open holes of telecom structure raises the background index by slightly larger number compared to visible case). These modeling results are consistent with those that use vertical sidewalls but depth-averaged dimensions. The good agreement between experiment and FDTD results, which assume ideal geometries and zero LER, suggests that the observed losses are intrinsic to the materials. Slight variabilities in the dimensions of the structures, the properties of the constituent materials, and the levels of control (such as uniformity and edge roughness) associated with the fabrication are the probable causes of the 10−15% overall discrepancy between experimental observation and FDTD simulation.

Conflict of Interest: The authors declare no competing financial interest.

Acknowledgment. The work was supported by a grant from the Office of Naval Research. We also gratefully acknowledge the contribution of Sandia National Laboratory which is a multiprogram laboratory operated by Sandia Corporation, a Lockheed Martin Company, for the United States Department of Energy under Contract DE-AC04-94AL85000 in fabricating large-area master mask using deep UV lithography (telecom) and electron beam lithography (visible). A.V.G. acknowledges support from the National Council of Science and Technology (CONACyT), the Secretariat of Public Education (SEP), and the Mexican Government.

Supporting Information Available: Supplementary Figures S1−S3 provide additional information for the results described throughout the main text. This material is available free of charge *via* the Internet at http://pubs.acs.org.

REFERENCES AND NOTES

1. Shelby, R. A.; Smith, D. R.; Schultz, S. Experimental Verification of a Negative Index of Refraction. *Science* **2001**, *292*, 77–79.
2. Schurig, D.; Mock, J. J.; Justice, B. J.; Cummer, S. A.; Pendry, J. B.; Starr, A. F.; Smith, D. R. Metamaterial Electromagnetic Cloak at Microwave Frequencies. *Science* **2006**, *314*, 977–980.
3. Yen, T. J.; Padilla, W. J.; Fang, N.; Vier, D. C.; Smith, D. R.; Pendry, J. B.; Basov, D. N.; Zhang, X. Terahertz Magnetic Response from Artificial Materials. *Science* **2004**, *303*, 1494–1496.
4. Paul, O.; Imhof, C.; Reinhard, B.; Zengerle, R.; Beigang, R. Negative Index Bulk Metamaterial at Terahertz Frequencies. *Opt. Express* **2008**, *16*, 6736–6744.
5. Dolling, G.; Enkrich, C.; Wegener, M. Low-Loss Negative-Index Metamaterial at Telecommunication Wavelengths. *Opt. Lett.* **2006**, *31*, 1800–1802.
6. Zhang, S.; Fan, W.; Panoiu, N. C.; Malloy, K. J.; Osgood, R. M.; Brueck, S. R. Optical Negative-Index Bulk Metamaterials Consisting of 2D Perforated Metal-Dielectric Stacks. *Opt. Express* **2006**, *14*, 6778–6787.
7. Shalaev, V. M. Optical Negative-Index Metamaterials. *Nat. Photonics* **2007**, *1*, 47.
8. Soukoulis, C. M.; Linden, S.; Wegener, M. Negative Refractive Index at Optical Frequencies. *Science* **2007**, *315*, 47–49.

9. Chanda, D.; Shigeta, K.; Gupta, S.; Cain, T.; Carlson, A.; Mihi, A.; Baca, A. J.; Bogart, G. R.; Braun, P. V.; Rogers, J. A. Large-Area Flexible 3D Optical Negative Index Metamaterial Formed by Nanotransfer Printing. *Nat. Nanotechnol.* **2011**, *6*, 402–407.
10. Zhang, S.; Fan, W.; Malloy, K. J.; Brueck, S. R. J.; Panoiu, N. C.; Osgood, R. M. Near-Infrared Double Negative Metamaterials. *Opt. Express* **2005**, *13*, 4922–4930.
11. Valentine, J.; Zhang, S.; Zentgraf, T.; Ulin-Avila, E.; Genov, D. A.; Bartal, G.; Zhang, X. Three-Dimensional Optical Metamaterial with a Negative Refractive Index. *Nature* **2008**, *455*, 376–380.
12. Garcia-Meca, C.; Hurtado, J.; Marti, J.; Martinez, A. Low-Loss Multilayered Metamaterial Exhibiting a Negative Index of Refraction at Visible Wavelengths. *Phys. Rev. Lett.* **2011**, *106*, 067402.
13. Chou, S. Y.; Krauss, P. R.; Renstrom, P. J. Nanoimprint Lithography. *J. Vac. Sci. Technol., B* **1996**, *14*, 4129–4133.
14. Xia, Y.; Rogers, J. A.; Paul, K. E.; Whitesides, G. M. Unconventional Methods for Fabricating and Patterning Nanostructures. *Chem. Rev.* **1999**, *99*, 1823–1848.
15. Gates, B. D.; Xu, Q.; Love, J. C.; Wolfe, D. B.; Whitesides, G. M. Unconventional Nanofabrication. *Annu. Rev. Mater. Res.* **2004**, *34*, 339–372.
16. Dolling, G.; Wegener, M.; Linden, S. Realization of a Three-Functional-Layer Negative-Index Photonic Metamaterial. *Opt. Lett.* **2007**, *32*, 551–553.
17. Wu, W.; Kim, E.; Ponizovskaya, E.; Liu, Z.; Yu, Z.; Fang, N.; Shen, Y. R.; Bratkovsky, A. M.; Tong, W.; Sun, C.; *et al.* Optical Metamaterials at Near and Mid-IR Range Fabricated by Nanoimprint Lithography. *Appl. Phys. A: Mater. Sci. Process.* **2007**, *87*, 143–150.
18. Bailey, T.; Choi, B. J.; Colburn, M.; Meissl, M.; Shaya, S.; Ekerdt, J. G.; Sreenivasan, S. V.; Willson, C. G. Step and Flash Imprint Lithography: Template Surface Treatment and Defect Analysis. *J. Vac. Sci. Technol., B* **2000**, *18*, 3572.
19. Hua, F.; Sun, Y.; Gaur, A.; Meitl, M.; Bilhaut, L.; Rotkina, L.; Wang, J.; Geil, P.; Shim, M.; Rogers, J. A. Polymer Imprint Lithography with Molecular-Scale Resolution. *Nano Lett.* **2004**, *4*, 2467–2471.
20. Hua, F.; Gaur, A.; Sun, Y.; Word, M.; Niu, J.; Adesida, I.; Shim, M.; Rogers, J. A. Processing Dependent Behavior of Soft Imprint Lithography on the 1−10 nm Scale. *IEEE Trans. Nanotechnol.* **2006**, *5*, 301–308.
21. Han, J.; Yeom, J.; Mensing, G.; Joe, D.; Masel, R. I.; Shannon, M. A. Surface Energy Approach and AFM Verification of the $(CF)_n$ Treated Surface Effect and Its Correlation with Adhesion Reduction in Microvalves. *J. Micromech. Microeng.* **2009**, *19*, 085017.
22. Hill, D. N.; Lee, J. D.; Cochran, J. K.; Chapman, A. T. Vapour Deposited Cone Formation during Fabrication of Low Voltage Field Emitter Array Cathodes. *J. Mater. Sci.* **1996**, *31*, 1789–1796.
23. Lee, H.; Park, Y.; Kim, J.; Choi, J.; Kim, J. Investigation of the Formation Mechanism of Spindt-Type Cathode by Simulation and Experiments. *J. Vac. Sci. Technol., B* **1999**, *17*, 547–551.
24. Smith, D. R.; Schultz, S.; Markos, P.; Soukoulis, C. M. Determination of Effective Permittivity and Permeability of Metamaterials from Reflection and Transmission Coefficients. *Phys. Rev. B* **2002**, *65*, 195104.
25. Chen, X.; Grzegorczyk, T. M.; Wu, B.; Pacheco, J. J.; Kong, J. A. Robust Method To Retrieve the Constitutive Effective Parameters of Metamaterials. *Phys. Rev. E* **2004**, *70*, 016608.
26. Smith, D. R.; Vier, D. C.; Koschny, T.; Soukoulis, C. M. Electromagnetic Parameter Retrieval from Inhomogeneous Metamaterials. *Phys. Rev. E* **2005**, *71*, 036617.
27. Maas, R.; Parsons, J.; Engheta, N.; Polman, A. Experimental Realization of an Epsilon-Near-Zero Metamaterial at Visible Wavelengths. *Nat. Photonics* **2013**, *7*, 907–912.
28. Burgos, S. P.; deWaele, R.; Polman, A.; Atwater, H. A. A Single-Layer Wide-Angle Negative-Index Metamaterial at Visible Frequencies. *Nat. Mater.* **2010**, *7*, 407–412.